ADVANCED QUANTUM TECHNOLOGIES
www.advquantumtech.com

Noise Performance of On-Chip Nano-Mechanical Switches for Quantum Photonics Applications

*Rodrigo A. Thomas, Celeste Qvotrup, Zhe Liu, and Leonardo Midolo**

Nano-opto-electromechanical systems provide an elegant solution for controlling light in quantum photonic integrated circuits, enabling small footprint devices for on-chip unitary transformations with low power consumption and cryogenic compatibility. In quantum applications, the noise of optical switches and routers is an important factor in establishing high-fidelity linear optical operations. In this work, the dynamical operation and noise performance of gap-variable directional couplers fabricated in Gallium Arsenide, are reported. The noise contribution stemming from mechanical modes of the devices are investigated and a low-temperature total phase noise of $\delta\phi \simeq (4.7 \pm 0.1)$mrad is observed over the 1–5 MHz bandwidth. The noise characteristic depends very weakly on the temperature, suggesting that the origin of noise stems primarily from electrostatic actuation.

1. Introduction

Reconfigurable photonic integrated circuits play an essential role in the development of photonic quantum information processing:[1] they enable programming arbitrary unitary transformations of qubits in dual-rail encoding,[2,3] switching and routing photons,[4] adjusting the resonant wavelength of resonators,[5] and controlling light-matter interaction with quantum emitters.[6] Nano-opto-electro-mechanical systems (NOEMS) have emerged recently as key technology to implement reconfigurable photonics both in the classical and in the quantum domains.[7–10] NOEMS provide an effective electro-optic interaction mediated by nano-mechanical motion, allowing unprecedented small footprints and ultra-low power consumption, without the need for electro-optic materials.[11] Silicon and III-V photonic circuits can thus be equipped with reconfigurable elements that do not rely on traditional thermo-optic or carrier injection phase-shifters.

In quantum technology, the use of NOEMS is gaining more attention as the need for low-loss and cryogenic-compatible devices is pivotal for loss-tolerant quantum algorithms. NOEMS achieve an effective phase shift ϕ by means of mechanical motion controlled by an applied bias voltage V.[12–14] Depending on the specific implementation and geometry, an effective electro-optic transduction $\phi(V)$, mediated by mechanical motion, can be implemented. For more details on specific implementations, we refer the reader to ref. [7].

While much attention has been devoted to the performance of NOEMS in terms of achievable phase shift range per unit Volt, or in terms of speed and repeatability, significantly less focus has been put into the characterization of device noise. Noise in NOEMS[15] originates primarily from thermo-mechanical oscillations and charge fluctuations in the device or in the driving electronics. Such stochastic noise is radically different than static imperfections or slow drifts in phase, as it cannot be corrected by a re-calibration of the device.[16] It is also expected that noise in NOEMS could be much higher than, e.g., thermo-optic or Pockels-effect devices, due to the presence of several mechanical modes responding to fluctuating forces. These mechanical oscillating modes, whose resonances (for NOEMS) typically fall in the few-MHz range, are slow compared to the time it takes for photons to travel across the device, but will add, on average, a random imprecision to the phases of each tunable element. When scaling up to large multi-mode interferometers, the imprecision of each element will therefore impact the overall fidelity of the unitary transformation.

In this work, we report on the performance of NOEMS directional couplers in terms of their dynamical behavior and noise performance, both at room and cryogenic temperatures, with the goal of modeling and estimating the noise of a device and its origin. We are not concerned with slow, i.e. >1 µs phase drifts, which can be, in principle, dynamically adjusted on-the-fly, but rather examine the higher frequency response due to the mechanical resonances in the devices.

2. Theoretical Background

The device characterized in this work is a gap-variable directional coupler, shown in **Figure 1a**, which is an improved version of previously-reported single-photon router reported in ref. [17].

R. A. Thomas, C. Qvotrup, Z. Liu, L. Midolo
Center for Hybrid Quantum Networks (Hy-Q)
Niels Bohr Institute
University of Copenhagen
Blegdamsvej 17, DK-2100 Copenhagen, Denmark
E-mail: midolo@nbi.ku.dk

The ORCID identification number(s) for the author(s) of this article can be found under https://doi.org/10.1002/qute.202400012

DOI: 10.1002/qute.202400012

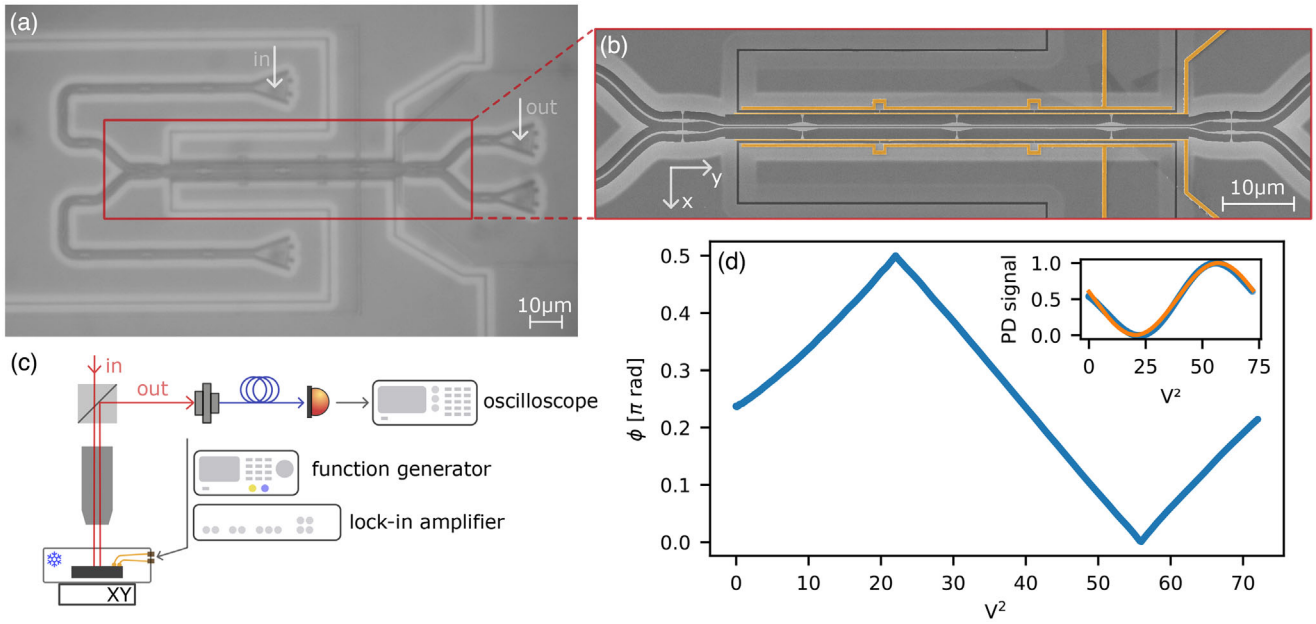

Figure 1. Characterization of on-chip nanomechanical directional couplers. a) Optical microscope image of the device, showing input and output gratings for light excitation and collection. b) Scanning electron microscope image of the directional coupler. Electrodes are highlighted in yellow. c) Schematic view of the experimental setup. The sample is mounted in a He flow cryostat and light is coupled to the chip via an objective. d) Phase response of the device versus voltage squared. The inset shows the photodetector (PD) signal before conversion to phase (blue line) and the fit to a cosine function (yellow line).

Gap-variable symmetric directional couplers are equivalent to Mach-Zehnder interferometers with a variable phase shifter on one arm. Here, the phase ϕ is given by the product gL, with g being the (displacement-dependent) coupling strength between the two waveguides forming the directional coupler, and L being the length of coupling section. The phase can be tuned by electrostatic forces acting on two pairs of thin metallic strips (highlighted in yellow in Figure 1b), which control the distance (and the coupling) between the waveguides.[7]

According to coupled-mode theory,[18] the coupling strength g follows an exponential dependence on the distance between the two waveguides, owing to the evanescent nature of the coupling:

$$g(u) = g_0 e^{-\kappa u} \tag{1}$$

where g_0 is the coupling without deformation, κ is the optical attenuation constant outside of the waveguide (evanescent tail), and u is the in-plane displacement along the x-axis (see Figure 1b for the axis orientation). In our directional couplers, $g_0 \simeq 1.1\ \mu m^{-1}$ and $\kappa \simeq 12\ \mu m^{-1}$, according to numerical simulations.[17] The out-of-plane displacement can be neglected, as long as it is small compared to the waveguide thickness.

We linearize the phase ϕ around a static deformation u_0, assuming a small deformation $\delta u(t)$:

$$\phi(t) \simeq \phi(u_0)(1 - \kappa \delta u(t)) \tag{2}$$

where $\phi(u_0) = g(u_0)L$ is the static phase which determines the splitting ratio of the directional coupler.

The electrostatic force, which governs the waveguide motion, scales with the square of the applied voltage V and is non-linear with respect to the mechanical deformation. We denote the in-plane motion of the electrode metal strip with q (to distinguish it from the waveguide motion u) and linearize again the force around a static displacement q_0 via a Taylor series:

$$F_e(t) \simeq \frac{1}{2} C'(q_0) V^2(t) + C''(q_0) \delta q V^2(t) + \cdots \tag{3}$$

where $C'(q_0)$ represents the electro-mechanical transduction efficiency, given by the change in capacitance C due to a static displacement and $C''(q_0)$ is the second derivative of the capacitance, responsible for spring softening.[19] According to finite element analysis of the electrode design of Figure 1a, $C'(q_0) \simeq 3\ \mathrm{nNV}^{-2}$.

The mechanical response of the directional coupler to an external force can be decomposed according to the overlap integral of the deformation profile with the mechanical modes of the device. Given the extended geometry of the device, each mechanical mode with mass m_i will contribute to the phase shift and to the electromechanical transduction with $\phi_i(u_o)$ and η_i, respectively. When considering the dynamics of the device around the steady state position u_0, the susceptibility

$$\chi_i(\omega) = \frac{1}{m_i} \frac{1}{\omega_i^2 - \omega^2 + i\gamma_i \omega} \tag{4}$$

dictates how each mode reacts to an external force that displaces the waveguide at a particular Fourier frequency ω. Here, the i-th mechanical mode has natural angular frequency ω_i and damping rate $\gamma_i = \frac{\omega_i}{Q_i}$, related to the mechanical quality factor Q_i. We

calculate the effective mass of each mode from their total 3D displacement $d(\mathbf{r})$ as

$$m_i = \int \rho(\mathbf{r}) \left| \frac{d(\mathbf{r})}{d_{\max}} \right|^2 dV \tag{5}$$

where ρ is the density of the materials (5.32 and 19.3 gcm^{-3} for GaAs and Au, respectively).

We assume the origin of the noise stems mainly from fluctuations due Brownian motion (thermo-mechanical forces) F_t and from electrostatic actuation (electro-mechanical forces) F_e. The former follows a dependence on the temperature T according to the fluctuation-dissipation theorem, i.e., $S_{FF,i} = 2m_i\gamma_i k_B T$, where k_B is the Boltzmann constant.

Assuming a noisy voltage source $V(t) = V_0 + \delta V(t)$, and neglecting small terms in the order of $\delta V(t)^2$, we obtain the total power spectral density of the phase noise:

$$S_{\phi\phi}(\omega) = \kappa^2 \sum_i |\phi_i(u_0)\chi_i(\omega)|^2 \left(S_{FF,i} + |\eta_i C'(u_0) V_0|^2 S_{VV}(\omega) \right) + S_{\text{light}} \tag{6}$$

where S_{VV} is the voltage flucutation noise and S_{light} is the shot noise from the laser used to probe the device. We note that the phase noise due to electrostatic actuation is expected to grow with the applied bias V_0, indicating that noise can be minimized for designs, which require small applied bias to achieve an equivalent phase shift. As the device should be designed to perform at least a π phase shift, one can expect the maximum root mean square (rms) electromechanical noise to be proportional to the figure of merit $V_\pi L$, where V_π is the static voltage required to achieve a full π phase shift.

3. Device Characterization

The sample is fabricated on a semi-insulating, non-intentionally doped, GaAs substrate with a 160nm -thick GaAs membrane, grown by molecular beam epitaxy on top of a thick AlGaAs (75% Al fraction) sacrificial layer. The fabrication procedure is described in detail in refs. [17, 20]. To achieve a larger tuning range, we extended the total coupling length $L = 60$ µm of the directional coupler by designing three cascaded actuators connected in parallel to two pairs or electrodes. The longer coupling section and the longer input–ouput waveguide section are expected to increase the total insertion loss of the coupler slightly, to ≈ 1.1 dB, considering a typical loss per unit length of 7 dBmm^{-1}.[17] Each of the three sections of the device is made of a 20-µm-long and 280-nm-wide movable electrode anchored via short tethers to the bulk of the membrane and to 220-nm-wide waveguides. The waveguides are tapered to a 500 nm width at the tether position to reduce optical scattering. The design allows us to extend the total length L of a single directional coupler without reducing the actuation speed or the device stiffness. The distance between the waveguides is approximately 120 nm, while the air gap between electrode is 280 nm. The electrodes (highlighted in yellow in Figure 1b) are connected to large bonding pads and interfaced to a printed circuit board mounted inside a He-flow cryostat, with a temperature control. The sample is kept in vacuum throughout the entire experiment to allow cryogenic cooling.

The experimental setup is shown in Figure 1c. Light from a continuous wave tunable laser (Toptica CTL 950) is coupled to one of the input gratings[21] via a room-temperature (295 K) objective and collected from another output grating via the same objective, as marked in Figure 1a. The output port is fiber-coupled to a fast photodiode (Thorlabs APD130A), which measures the modulated intensity $I(t) = I_0 \cos^2(\phi(t))$. We drive the NOEMS electrodes with a function generator (Rigol DG1032Z) and acquire the signal from the photodiode with an oscilloscope (Rigol DG1054Z). The Figure 1d (inset) shows a typical signal collected at noted the output port while slowly sweeping the static voltage V_0, plotted as a function of $V_0^2 \propto F_e$ at room temperature, where a full π-rotation is achieved with $V_0 = V_\pi = 8.5$V. The corresponding phase ϕ is plotted (in the range $[0, \pi/2]$ in Figure 1d, from which we extract a phase sensitivity of 45 mrad/V^2 and a figure of merit $V_\pi L = 0.05(1)$ V · cm. In dual-rail encoding of photonic qubits, such gate allows performing arbitrary 2π rotations along one of the Bloch vectors.

3.1. Driven Response

We start analyzing the dynamical response in the presence of a small sinusoidal driving voltage superimposed with a static bias offset. A lock-in amplifier (Zurich Instruments HF2LI 50 MHz) is used to drive the device and measure the transmitted light intensity collected at the photodiode. In **Figure 2a**, the amplitude squared R^2 and the phase θ of the optical signal are shown for a range of the driving RF frequency, with driving signal $V(t) = V_0 + V_1 \sin(\omega t)$, where $V_0 = 0.5$ V and $V_1 = 1$ mV. Three resonances are clearly visible, corresponding to the fundamental in-plane mechanical motion of the device. The displacement profile of the modes is shown in Figure 2c–f. The modes (c) and (d) are simulated to have a natural frequency of approximately 1310 kHz, while (e) and (f) are at 1370 kHz. We attribute the small variations in mechanical resonances to fabrication imperfections as strain induced by the metal lines and waveguide width variations.

The measurement allows us to probe the susceptibility $\chi(\omega)$ for three nearby mechanical modes. The data, collected with the sample at room temperature, is fitted with the model of Equation (4), where we extract the line-widths (or equivalently the mechanical Q factors) and resonant frequency for each mode.

A slow cool-down of the sample is done while measuring the temperature and performing a continuous frequency scan with the lock-in amplifier. A scan is acquired every 25 s and fitted to extract the frequency and line-width dependence on temperature of mode (1) from Figure 2a. The results are shown in Figure 2b. A linear decrease of the resonant frequency with temperature at a rate of approximately -2 kHzK^{-1} is observed. We attribute this effect to a thermal stress in the electrodes region, caused by the large coefficient of thermal expansion of gold compared to GaAs. While cooling down, a tensile stress is created, which causes an increase of the device stiffness. Mechanical linewidths are instead rather constant at room temperature (around 1 kHz) only to drop by a roughly factor of three in the range 150–50 K, reaching a limit of ≈ 0.25 kHz. The Q factor in our structure is

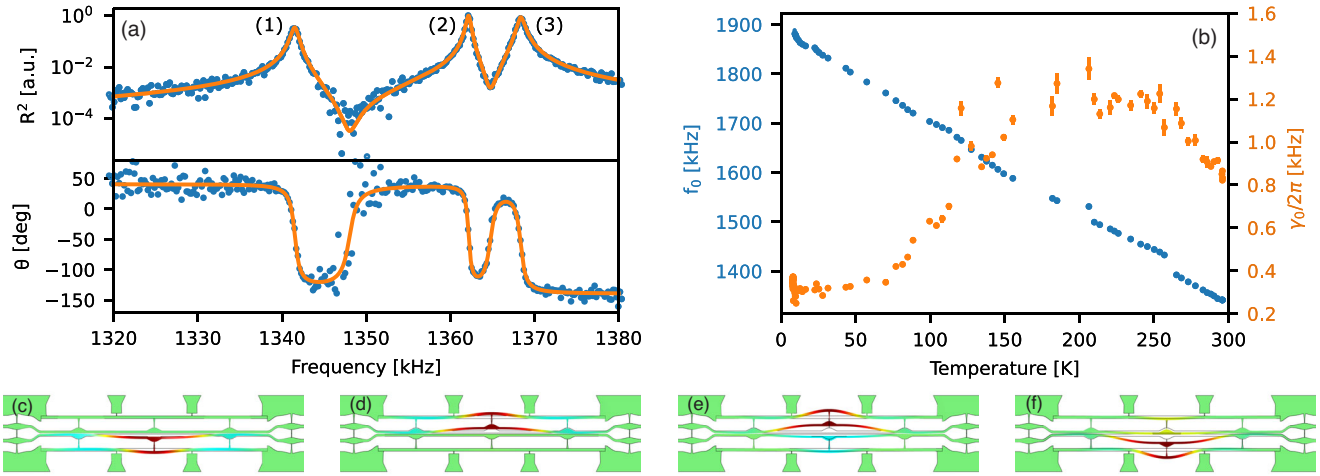

Figure 2. Phase-sensitive optical response of the device to a weak RF drive. a) Amplitude squared (R^2) and phase (θ) from the transmitted light signal, demodulated at the drive RF frequency. b) Tracking the resonant frequency and damping rate γ_i of mode (1) as a function of temperature. The error bars in the damping rate correspond to one standard deviation. c–f) show the simulated displacement profiles of the fundamental modes of the structure.

limited by clamping losses[22] and thermoelastic damping,[23] which are predominant at low and high temperatures, respectively. We suspect that the increase in linewidth at ≈ 200 K is the result of the interplay of thermal stress on the structure and thermoelastic damping. Further insight is needed to model the linewidth dependence on temperature.

The natural frequency of the modes and their linewidths are also varying depending on the static applied bias V_0. **Figure 3**a,b shows the mechanical frequency shift and resonance linewidth, respectively, for the three fundamental resonances at room temperature. The frequency shift is the combined result of the geometric deformation of the electrodes and the back action of the electrostatic force (second term in Equation (3)).[24] Each mode shifts proportionally to V^2 but at different rates depending on their overlap η_i with the electrostatic force.

The cause of the increase in resonance linewidths (Figure 3b) is not known and would require a more in-depth analysis. We speculate that the electrostatic force could exhibit an additional term, in quadrature with the velocity $\delta u'(t)$, which might originate from a parasitic impedance. Such impedance would cause a delay in the redistribution of charges across the electrical circuit driving the actuator and thus would act as an effective damper for the mechanical oscillator. The parasitic impedance could stem either from the experimental setup (cables, printed circuit boards, etc), or from other devices connected in parallel to the one under test.

3.2. Noise Characterization

To measure the phase noise, we convert the optical intensity spectrum from the photodiode to a phase spectrum. We set the bias voltage V_0 such that the derivative of the intensity response is maximum, i.e., when the intensity is most sensitive to phase fluctuations, which provides direct conversion to phase $\delta\phi(t) = \delta I(t)/I_0$. The measured power spectral density (PSD) of phase noise is shown in **Figure 4** at room (295 K) and cryogenic (10 K) temperature. Due to unavoidable shifts in the device opto-electromechanical response during cooldown, caused by refractive index changes and thermal stresses, the bias voltage V_0 is slightly

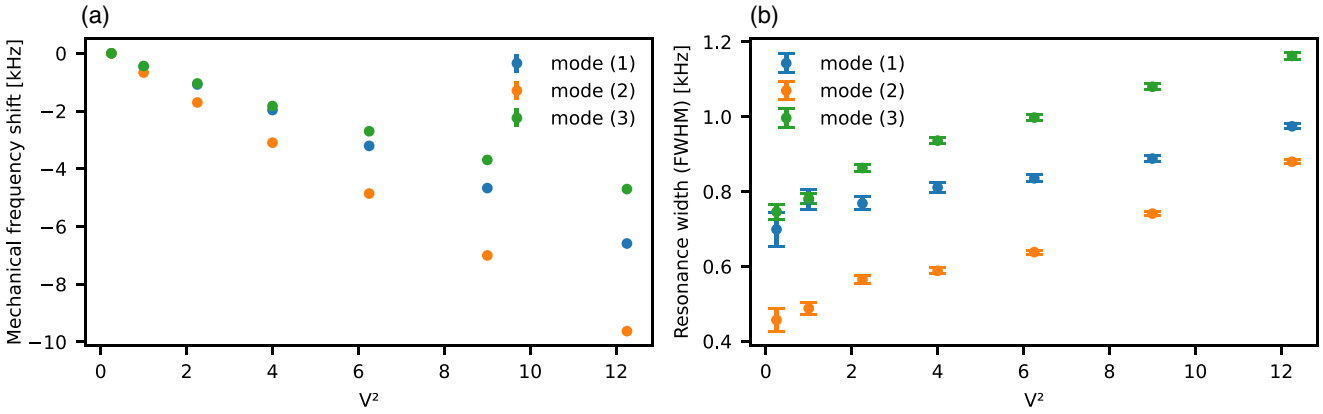

Figure 3. Tracking the frequency shift and dampening of the mechanical modes versus set voltage. As the voltage increases from 0.5 to 3.5 V, the modes shift down in frequency (a) and are damped (b) approximately proportionally to V^2. The error bars in the damping rate correspond to 1 standard deviation.

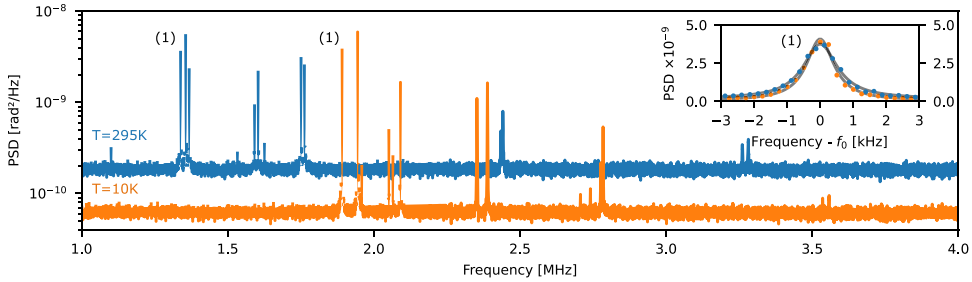

Figure 4. Calibrated phase noise spectra. A continuous wave (CW) laser probes the mechanical fluctuations of the switch at the half-fringe setting at 295 (blue) and 10 K (yellow). The power spectral density (PSD) of intensity fluctuations in the output light is composed of photon shot-noise and optically transduced mechanical noise. Inset: zoom at the peaks labeled as (1) overlaid with a Lorentzian fit. The resonant frequency f_0 is 1339 kHz (1891 kHz) at $T = 295$K (10 K). Each spectrum is the average of 60 independent traces.

different in the two cases, i.e., 5 and 4.5 V at room and cryogenic temperature, respectively.

Besides the group of fundamental resonance at ≈1.3 MHz, several higher-order resonances corresponding to various mechanical modes ranging up to 3.6 MHz are visible at both temperatures, with a clear shift to higher frequencies for the low-temperature case. We observe that every mechanical resonance consists of several closely spaced mechanical modes that roughly tune by over 600 kHz during cool-down, although with slightly different rates. The background phase noise S_{light} is attributed to shot noise from the laser and it changes slightly across the measurements due to optical realignment and change of grating efficiency. The peaks are fitted with Lorentzian curves (shown in the inset of Figure 4 for the peak marked with (1) at room and low temperature), to accurately estimate the area under the peak and subtract the background noise. A total integrated phase noise of 6.9(0.2) mrad and 4.7(0.1) mrad is measured at room and cryogenic temperatures, respectively.

To provide an interpretation of the measured noise, we consider the lowest frequency mechanical mode given by the in-plane vibration of a single waveguide coupled to the mechanical actuator whose integrated root-mean-square (rms) phase noise is 2.5(0.4) mrad. We plot the phase power spectral densities at room and cryogenic temperature of the mode in linear scale in the inset of Figure 4. It is evident that the noise is largely unaffected by the temperature change, which implies that electromechanical noise is dominating. Higher-order modes are instead visibly suppressed when reducing temperature, which indicates a smaller electromechanical coupling η_i in these modes. From finite element analysis of the modes (cf. Figure 2c–f) we estimate $m = 10$ pg, $\phi(u_0) = 5$ rad and $\eta = 0.062$, while from measurements $\gamma/(2\pi) = 0.94 \pm 0.02$ kHz. The equivalent thermal force spectral density at $T = 10$ K is roughly $\approx$ 0.05 fN/$\sqrt{\text{Hz}}$, resulting in ≈1.5 pm rms effective motion amplitude and a phase noise of only about $\delta\phi_{rms} = 0.2$ mrad. The measured total phase noise is thus an order of magnitude higher, requiring a force spectral density in the order of a few fN/$\sqrt{\text{Hz}}$, which according to our analysis can be attributed to noise in the electromechanical transduction. Based on Equation (6) and the finite element analysis, we estimate the voltage source spectral noise to be in the order of $\delta V \approx$ 0.5 μV/$\sqrt{\text{Hz}}$. However, we measured the spectral noise stemming from our voltage source to be significantly lower, approximately around $\approx$ 20nV/$\sqrt{\text{Hz}}$, as commonly reported by most digital to analog converters in the absence of amplifiers. It is therefore unlikely that the voltage source is the origin of noise.

We suspect that additional noise is originated directly in the sample. A possible source of noise that is not temperature-dependent is the shot noise due to leakage currents between the device electrodes. Such current, typically of few nA, could originate at the metal-semiconductor interface and flow across the thin GaAs tethers supporting the electrodes, due to the lack of surface passivation or isolation with high dielectric constants (high-κ dielectrics). Consequently, the noise could be significantly reduced with different materials or electrical isolation geometries. Quantifying the magnitude of the effect and identifying the methods for suppressing it is currently an ongoing effort.

4. Conclusion

We have reported on a measurement of the dynamical response and phase noise in NOEMS tunable devices for quantum photonic application. The total phase noise at cryogenic operation is 4.7 ± 0.1 mrad, under a static bias of $V_0 = 4.5$ V, from which we estimate a maximum noise of 8.8 ± 0.2 mrad at $V_0 = V_\pi = 8.5$ V. Such worst-case scenario noise would correspond to a single Pauli-X gate error of $7.7 \cdot 10^{-5}$, or equivalently a eight-bit precision in phase encoding (given by $n = \log_2(\delta\phi/\pi)$). For comparison, Silicon thermo-optic phase shifters in Mach-Zehnder interferometers exhibit an extinction rate of over -60 dB, corresponding to an upper bound of phase noise in the <1 mrad range.

Tunable directional couplers and tunable phase shifters based on NOEMS could replace thermo-optic phase shifters in fully GaAs-based linear optical quantum circuits, that include QDs as single photon sources. Large multi-mode universal unitary gates with N inputs/outputs can be built cascading networks of $O(N^2)$ devices in rectangular or triangular (Haar) configurations. While the obvious advantages would be faster reconfigurability, low-power consumption and low cross-talk, compared to the thermo-optic counterpart, the issue of noise affects the overall precision of the circuit as the number of modes and gates increases. We note that the noise observed here is slow compared to the time that the photon takes to traverse the circuit. Thus, while a single shot experiment would not be sensitive to the mechanical resonances of NOEMS, any subsequent run will undergo slightly different unitary transformations. We can assume the deviations to be only weakly correlated in time (and thus fully random)

although developing better Q factor resonators, might result in coherent oscillation over the sampling period, which can be in principle treated as a predictable offset and corrected for. Additional analysis, beyond the scope of the current work, is needed to provide an in-depth theoretical investigation of the impact of noise and correction strategies in NOEMS-based linear optical quantum gates. Here, we refer to a previous theoretical analysis,[25] which has shown that the eight-bit phase resolution reported here enables near-unity fidelity operations for over 50-mode gates, consisting of thousands of phase shifters. Therefore, we conclude that, despite the mechanical resonances, NOEMS are an excellent choice for low-noise reconfigurable unitary gates, offering a performance comparable with traditional thermo-optic devices. For even larger architectures, it is desirable to push the noise further, reaching single gate errors below 10^{-6}, or 12-bit precision. Potential avenues to further improve the noise are to further reduce the overall device length and employ ultra-low noise voltage sources with $\mathrm{nV}/\sqrt{\mathrm{Hz}}$. Techniques as surface passivation or electrode deposition with a high-κ dielectric such as aluminum or hafnium oxide, could strongly suppress leakage currents and the shot-noise associated to it. Finally, if sensitive measurements of phase could be implemented directly on-chip, active feedback techniques could be employed to selectively dampen the fundamental mechanical modes, at the expense of device complexity.

Acknowledgements

The authors acknowledged Nicolas R. H. Pedersen and Andrea González Boa for their contributions to the experimental setup. The authors acknowledged funding from the European Research Council (ERC) under the European Union's Horizon 2020 research and innovation program (No. 949043, NANOMEQ), the Danish National Research Foundation (Center of Excellence "Hy-Q," grant number DNRF139), and Styrelsen for Forskning og Innovation (FI) (5072- 00016B QUANTECH).

Conflict of Interest

The authors declare no conflict of interest.

Data Availability Statement

The data that support the findings of this study are available from the corresponding author upon reasonable request.

Keywords

micro- and nano-opto-electro-mechanical systems, photonic integrated circuits, quantum photonics

Received: January 8, 2024
Revised: April 17, 2024
Published online: May 22, 2024

[1] F. Flamini, N. Spagnolo, F. Sciarrino, *Rep. Prog. Phys.* **2018**, *82*, 016001.
[2] J. Bao, Z. Fu, T. Pramanik, J. Mao, Y. Chi, Y. Cao, C. Zhai, Y. Mao, T. Dai, X. Chen, X. Jia, L. Zhao, Y. Zheng, B. Tang, Z. Li, J. Luo, W. Wang, Y. Yang, Y. Peng, D. Liu, D. Dai, Q. He, A. Muthali, L. Oxenløwe, C. Vigliar, S. Paesani, H. Hou, R. Santagati, J. Silverstone, A. Laing, et al., *Nat. Photonics* **2023**, *17*, 573.
[3] N. C. Harris, G. R. Steinbrecher, M. Prabhu, Y. Lahini, J. Mower, D. Bunandar, C. Chen, F. N. Wong, T. Baehr-Jones, M. Hochberg, S. Lloyd, D. Englund, *Nat. Photonics* **2017**, *11*, 447.
[4] P. I. Sund, E. Lomonte, S. Paesani, Y. Wang, J. Carolan, N. Bart, A. D. Wieck, A. Ludwig, L. Midolo, W. H. Pernice, P. Lodahl, F. Lenzini, *Sci. Adv.* **2023**, *9*, eadg7268.
[5] A. W. Elshaari, W. Pernice, K. Srinivasan, O. Benson, V. Zwiller, *Nat. Photonics* **2020**, *14*, 285.
[6] C. P. Dietrich, A. Fiore, M. G. Thompson, M. Kamp, S. Höfling, *Laser Photonics Rev.* **2016**, *10*, 870.
[7] L. Midolo, C. Qvotrup, *Photon. Quantum Techn.: Sci. Appl.* **2023**, *2*, 581.
[8] N. Quack, H. Sattari, A. Y. Takabayashi, Y. Zhang, P. Verheyen, W. Bogaerts, P. Edinger, C. Errando-Herranz, K. B. Gylfason, *IEEE J. Quantum Electron.* **2019**, *56*, 1.
[9] C. Errando-Herranz, A. Y. Takabayashi, P. Edinger, H. Sattari, K. B. Gylfason, N. Quack, *IEEE J. Sel. Top. Quantum Electron.* **2019**, *26*, 1.
[10] C. Haffner, A. Joerg, M. Doderer, F. Mayor, D. Chelladurai, Y. Fedoryshyn, C. I. Roman, M. Mazur, M. Burla, H. J. Lezec, V. A. Aksyuk, J. Leuthold, *Science* **2019**, *366*, 860.
[11] L. Midolo, A. Schliesser, A. Fiore, *Nat. Nanotechnol.* **2018**, *13*, 11.
[12] M. Poot, H. X. Tang, *Appl. Phys. Lett.* **2014**, *104*, 6.
[13] T. Liu, F. Pagliano, R. van Veldhoven, V. Pogoretskiy, Y. Jiao, A. Fiore, *Appl. Phys. Lett.* **2019**, *115*, 25.
[14] F. Beutel, T. Grottke, M. A. Wolff, C. Schuck, W. H. Pernice, *Opt. Express* **2022**, *30*, 30066.
[15] F. Mohd-Yasin, D. J. Nagel, C. E. Korman, *Meas. Sci. Technol.* **2009**, *21*, 012001.
[16] T. Rudolph, *APL Photonics* **2017**, *2*, 030901.
[17] C. Papon, X. Zhou, H. Thyrrestrup, Z. Liu, S. Stobbe, R. Schott, A. D. Wieck, A. Ludwig, P. Lodahl, L. Midolo, *Optica* **2019**, *6*, 524.
[18] L. Midolo, C. Qvotrup, *Nano-Opto-Electro-Mechanical Systems for Integrated Quantum Photonics*, chapter 21, John Wiley and Sons, Ltd, New York **2023**, pp. 581–597.
[19] G. De Pasquale, A. Somà, *Mech. Syst. Signal Process.* **2010**, *24*, 1621.
[20] L. Midolo, T. Pregnolato, G. Kiršanskė, S. Stobbe, *Nanotechnology* **2015**, *26*, 484002.
[21] X. Zhou, I. Kulkova, T. Lund-Hansen, S. L. Hansen, P. Lodahl, L. Midolo, *Appl. Phys. Lett.* **2018**, *113*, 25.
[22] G. D. Cole, I. Wilson-Rae, K. Werbach, M. R. Vanner, M. Aspelmeyer, *Nat. Commun.* **2011**, *2*, 231.
[23] R. Lifshitz, M. L. Roukes, *Phys. Rev. B* **2000**, *61*, 5600.
[24] S. Kalicinski, H. Tilmans, M. Wevers, I. De Wolf, *Sensors and Actuators A: Physical* **2009**, *154*, 304.
[25] M. Y. Saygin, I. Kondratyev, I. Dyakonov, S. Mironov, S. Straupe, S. Kulik, *Phys. Rev. Lett.* **2020**, *124*, 010501.